Impedance-Based Characterization and Experimental Stability Analysis of Grid-Forming Converters with Virtual Admittance Control

Dominik Schulz[1]*, Lucas Ehrlich[1], Rüdiger Schwendemann[1], Andreas Liske[1], Marc Hiller[1]
1 Institute of Electrical Engineering (ETI), Karlsruhe Institute of Technology (KIT), Karlsruhe, Germany
*dominik.schulz@kit.edu

***Abstract*—Grid-connected power converters increasingly utilize grid-forming (GFM) control to enhance system stability and support a high penetration of power electronics. However, GFM converters can introduce instabilities in strong grids and interact with neighboring converters. Suitable modeling approaches, such as impedance-based methods, can help assess and mitigate these stability issues. This paper develops a comprehensive impedance model for GFM converters based on virtual admittance control, which has recently attracted significant research interest. The impact of key control parameters on impedance characteristics is investigated. The impedance model is validated through experimental impedance measurements. Insights derived from the model are further used to assess and mitigate converter interactions in laboratory experiments.**

***Index Terms*—grid-forming control, converter impedance, stability analysis, impedance measurement**

I. Introduction

As the energy transition progresses, an increasing number of power converters are connected to the grid. Recently, there has been a growing demand for these units to operate in grid-forming (GFM) mode to replace decommissioned synchronous machines and their desired properties, such as inertia. However, these developments can result in instabilities in strong grids and interactions among power converters [1]. To study and mitigate such interactions, the impedance-based stability criterion [2] is recognized as an effective approach and has already been studied extensively [3], [4]. The impedance-based analysis requires knowledge of the converter impedance, which can be obtained through black-box measurements when the control structure or parameters are unknown. If the control structure and system parameters are available, the converter impedance can also be derived analytically. The resulting impedance model provides insights into the influence of system parameters and the control structure. Among GFM control strategies, there is considerable variation in the control structures employed. Strategies for voltage control include direct synthesis, single-loop, and double-loop structures [5]. Most previous studies on GFM converter impedances focus on double-loop control with PI voltage control in the *dq*-frame [6]–[8], often extended by a virtual impedance loop [9], [10]. As an alternative, GFM controls based on virtual admittance (GFM-VA) [11] have recently gained interest due to their enhanced stability in strong grids and their ability to implement the virtual admittance without the derivative terms required in an equivalent virtual impedance formulation [12]–[15]. However, the converter output impedance is not considered in these works. Existing papers that study the output impedance [16], [17] do not take into account the impact that the control parameters have on the resulting converter output impedance. Moreover, the converter impedances are investigated using analytical and simulation models only. This paper contributes to this research by developing a comprehensive impedance model for GFM converters with virtual admittance control. The model is derived using a signal-flow graph that includes multiple-input multiple-output (MIMO) dynamics to capture frequency couplings. Based on this model, a sensitivity analysis is performed to identify the influence of key control parameters on the impedance characteristics. The model and its parameter sensitivities are experimentally validated through impedance measurements. Finally, the insights gained from the model are used to analyze and mitigate converter interactions in laboratory experiments.

II. Converter Impedance Modeling

A. Converter System and Control Structure

The general system studied in this paper is shown in Fig. 1. It consists of a two-level converter that is connected to the grid using an LCL filter. The DC link is controlled by an external source to enable the converter to provide grid-forming functionality. Relevant system parameters are listed in Table I.

An overview of the investigated converter control structure is given in Fig. 2. The power control loops (PC) use the power setpoints P_{set} and Q_{set} and the measured power to define the angle θ of the internal *dq*-frame, as well as the magnitude of the internal voltage setpoint v_{set}. The difference between this setpoint and the measured filter voltage v_c is passed to the

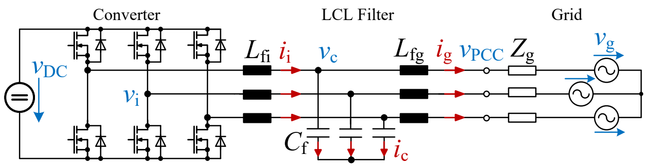

Fig. 1. Converter with DC source, LCL filter and grid connection

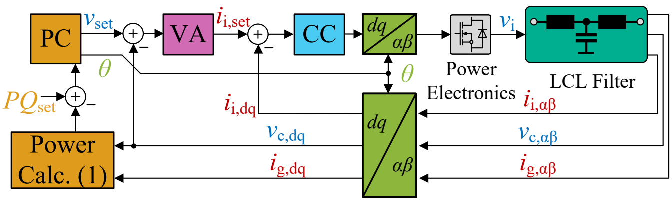

Fig. 2. Control structure overview of GFM control with VA

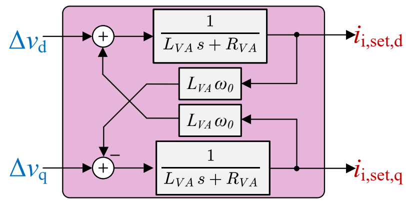

Fig. 4. Control structure detail of virtual admittance

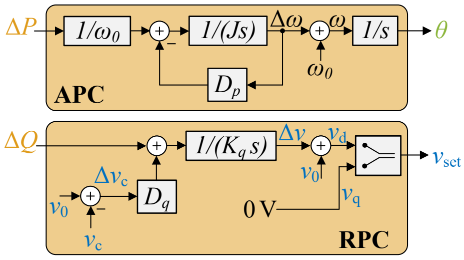

Fig. 3. Control structure detail of active and reactive power control

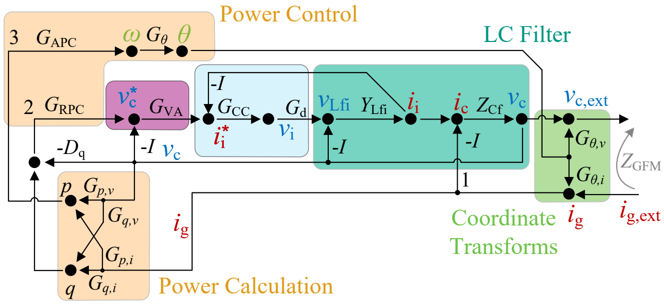

Fig. 5. Signal-flow graph of GFM control with VA

virtual impedance (VA), which calculates the resulting current setpoint $i_{\text{i,set}}$. The subordinate current controller (CC) then determines the converter output voltage v_i.

The power calculations are performed in the *dq*-frame:

$$P = \frac{3}{2}(v_d i_d + v_q i_q)$$
$$Q = \frac{3}{2}(v_q i_d - v_d i_q) \tag{1}$$

Fig. 3 illustrates the active and reactive power control in detail. The active power control (APC) implements a virtual synchronous machine with virtual inertia J, the damping term D_p, and the nominal fundamental frequency ω_0. This results in the swing equation (2) that defines the angular frequency ω and the internal *dq*-frame angle θ after integration.

$$\Delta P = \omega_0 J \frac{d\omega}{dt} + \omega_0 D_\text{p}(\omega - \omega_0) \tag{2}$$
$$\rightarrow \omega = \frac{1}{sJ}\left(\frac{\Delta P}{\omega_0} - D_\text{p}(\omega - \omega_0)\right) + \omega_0 \tag{3}$$

The reactive power control (RPC) must balance the control objectives for both the reactive power setpoint Q_set and the grid voltage setpoint v_0. This is due to the voltage drop introduced by the virtual admittance. The RPC compensates for this difference from the internal voltage setpoint v_set by tracking both the error in reactive power ΔQ and the voltage magnitude Δv_c:

$$v_\text{d} = \frac{1}{K_\text{q} s}(\Delta Q + D_\text{q}\Delta v_\text{c}) + v_0 \tag{4}$$

The virtual admittance (VA) control structure is shown in Fig. 4. It calculates the currents that result from applying the voltage difference Δv_dq between the internal voltage setpoint v_set and the measured capacitor voltage v_c across a virtual admittance. This virtual admittance consists of a virtual resistance R_VA and a virtual inductance L_VA with $G_\text{VA} = (R_\text{VA} + sL_\text{VA})^{-1}$. In contrast to GFM control structures with virtual impedance, no derivation of the current is required. The current setpoint determined by the VA is then passed to a current controller (CC). This is a conventional PI controller with a *dq*-decoupling term described by

$$\mathbf{v}^*_\text{i,dq} = (K_\text{p,CC} + K_\text{i,CC}/s)\,\Delta i_\text{i,dq} + \mathbf{J}\omega_0 L_\text{fi}\,\mathbf{i}^*_\text{i,dq}, \tag{5}$$

where $\mathbf{J}$ is the imaginary unit matrix.

Finally, the *dq*-quantities are transformed back to the stationary $\alpha\beta$-frame. After linearization [3], the small-signal impact of the transforms can be described by

$$\Delta v_\text{dq} = \begin{bmatrix} -v_\text{0,q} \\ +v_\text{0,d} \end{bmatrix} \Delta\theta = G_{\theta,v}\,\Delta\theta \quad \text{and} \tag{6}$$
$$\Delta i_\text{dq} = \begin{bmatrix} +i_\text{0,q} \\ -i_\text{0,d} \end{bmatrix} \Delta\theta = G_{\theta,i}\,\Delta\theta, \tag{7}$$

where v_0 and i_0 denote the steady-state operating point.

TABLE I
RELEVANT SYSTEM PARAMETERS

Parameter	Symbol	Value
Converter-side LCL inductance	L_fi	100 µH
Grid-side LCL inductance	L_fg	50 µH
LCL filter capacitance	C_f	13.5 µF
DC link voltage	v_DC	650 V
Switching and sampling frequency	f_sw	50 kHz

B. Impedance Derivation using Matrix Signal-Flow Graph

To derive the converter output impedance, a matrix signal-flow graph (SFG) of the control and filter system is constructed using the transfer functions given in the preceding paragraphs and depicted in Fig. 5.

The *forward return loop method* [18], [19] is applied to the SFG to determine the desired transfer function $Z_{\mathrm{GFM,dq}}(s)$ in the *dq*-frame:

$$\begin{aligned} Z_{\mathrm{GFM,dq}}(s) =& N_{vc}\, Z_{\mathrm{Cf}}\, N_{ig}\,(-1) + \\ & G_{\theta,v}\, G_{\theta}\, G_{\mathrm{APC}}\, G_{p,i}\, N_{ig} + \\ & N_{vc}\, Z_{\mathrm{Cf}}\, N_{ii}\, Y_{\mathrm{Lfi}}\, G_{\mathrm{d}}\, G_{\mathrm{CC}}\, G_{\mathrm{VA}}\, G_{\mathrm{RPC}} G_{q,i}\, N_{ig} \end{aligned} \tag{8}$$

The node factors are defined as:

$$N_{ii} = (I + Y_{\mathrm{Lfi}}\, G_{\mathrm{d}}\, G_{\mathrm{CC}})^{-1} \tag{9}$$

$$N_{ig} = (I + G_{\theta,i}\, G_{\theta}\, G_{\mathrm{APC}}\, G_{p,i})^{-1} \tag{10}$$

$$\begin{aligned} N_{vc} =& (I + Z_{\mathrm{Cf}}\, N_{ii}\, Y_{\mathrm{Lfi}} \\ & \cdot (I \ + \ G_{\mathrm{d}}\, G_{\mathrm{CC}}\, G_{\mathrm{VA}}\, (I + D_{\mathrm{q}} - G_{\mathrm{RPC}})))^{-1} \end{aligned} \tag{11}$$

Finally, the grid-side LCL inductance Z_{Lg} is added.

To obtain the impedance in the sequence domain, the reference frame transformations described in [3], [20] are applied:

$$Z_{\mathrm{GFM,pn}}(s) = A_{\mathrm{Z}}\, Z_{\mathrm{GFM,dq}}(s)\, A_{\mathrm{Z}}^{-1} \tag{12}$$

$$\text{with } A_{\mathrm{Z}} = \frac{1}{\sqrt{2}} \begin{bmatrix} 1 & j \\ 1 & -j \end{bmatrix} \tag{13}$$

Since the impedance in the *dq*-frame is not symmetrical due to the power control loops, the resulting converter impedances in the sequence domain will exhibit sequence and phase couplings. This prevents modeling the converter as having decoupled positive and negative sequence impedances. Instead, the multiple-input multiple-output (MIMO) characteristics of the converter must be described using an impedance matrix:

$$\begin{bmatrix} V_{\mathrm{p}}(s_+) \\ V_{\mathrm{n}}(s_-) \end{bmatrix} = \underbrace{\begin{bmatrix} Z_{\mathrm{pp}}(s) & Z_{\mathrm{pn}}(s) \\ Z_{\mathrm{np}}(s) & Z_{\mathrm{nn}}(s) \end{bmatrix}}_{Z_{\mathrm{GFM,pn}}(s)} \begin{bmatrix} I_{\mathrm{p}}(s_+) \\ I_{\mathrm{n}}(s_-) \end{bmatrix}, \tag{14}$$

where $s_+ = s + \omega_0$, $s_- = s - \omega_0$, and ω_0 is the fundamental frequency.

C. Parameter Influence on Analytical Converter Impedance

Fig. 6 shows impedance curves resulting from the derived model. The gray curve represents the default parameter case. At 50 Hz, the impedance exhibits a narrow peak and change in phase. Above this, at around 65 Hz, the virtual admittance causes a second, higher peak. The filter resonant frequencies ω_{LC} and ω_{LCL} are observed at 4.3 kHz and 7.5 kHz, respectively. The colored and dashed curves show the impact of selected control and filter parameters. Increasing the RPC parameter D_{q} affects the impedance curve around the fundamental frequency, as visible in the orange curve. Both the impedance magnitude and phase excursions at 65 Hz increase, and a second peak at the mirror frequency of 35 Hz appears. Reducing the value of the virtual inductance L_{VA} yields the violet curve. The influence is limited to frequencies below 100 Hz, where it reduces the impedance magnitude and moderates the peak and the phase transition at 65 Hz. Increasing the current controller proportional gain $K_{\mathrm{p,cc}}$ alters

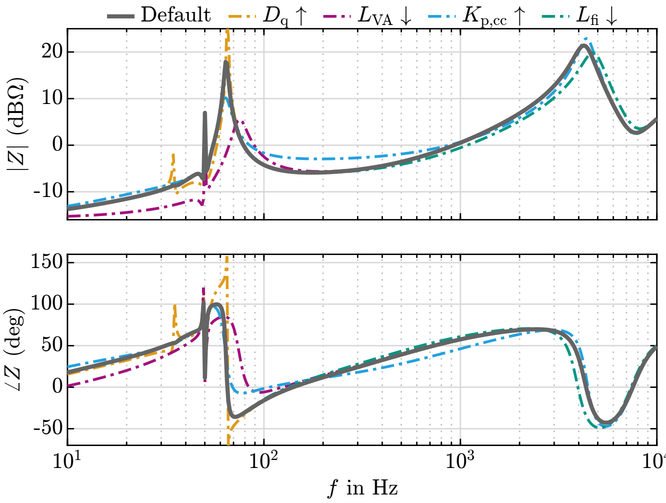

Fig. 6. Analytical positive sequence impedance curves with impact of control and filter parameters

the impedance curve in the frequency range up to approximately 1 kHz. The control parameters have a minimal effect on the frequency range near the LCL resonant frequencies, where the filter parameters have the primary impact. For instance, reducing the converter-side inductance L_{fi} shifts the resonant peak at ω_{LC} to higher frequencies.

III. Impedance Measurements

This section validates the derived impedance model through impedance measurements.

The grid-forming converter to be characterized as the device under test (DUT) is based on a previously developed system [21] using SiC MOSFETs with the hardware parameters given in Table I. The converter is shown in Fig. 7. The presented control structure shown in Fig. 2 is implemented on a Zynq™ 7030 SoC. The investigated control parameters can be tuned online, allowing for subsequent measurement runs without reprogramming the SoC. If not otherwise noted, the default control parameters given in Table II are used.

To measure the impedance of a grid-forming converter, it must be excited by a controllable current source. The measurement setup for this is shown in Fig. 7. The grid-forming DUT is connected to a coupling cabinet, which includes precision measurement equipment and a ferrite coupling inductance of $L_{\mathrm{cp}} = 100\,\mu\mathrm{H}$. The local interface current i_{g} is controlled through this inductance using a high-dynamics power amplifier. The current consists of the excitation at the investigated frequency and a fundamental frequency component, enabling measurements at the desired operating point.

The converter impedance is determined based on the converter voltage response to current excitations. To this end, the excitation current is controlled to an amplitude of $|i_{\mathrm{g,set}}| = 1\,\mathrm{A}$ in a frequency range from 10 Hz to 10 kHz. For a given frequency, the DUT is excited in both the positive and negative sequence, each with a phase shift of $\varphi \in \{0°, 120°, 240°\}$.

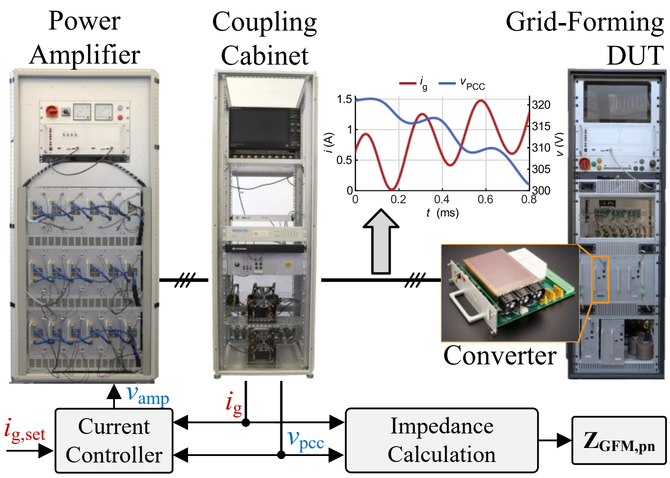

Fig. 7. Grid-forming converter impedance measurement setup

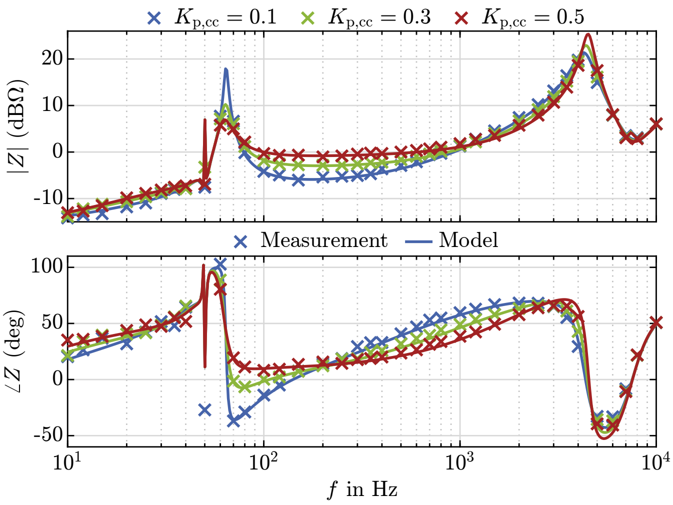

Fig. 8. Measured and modeled positive sequence impedance curves for variation of current controller gain $K_{p,cc}$

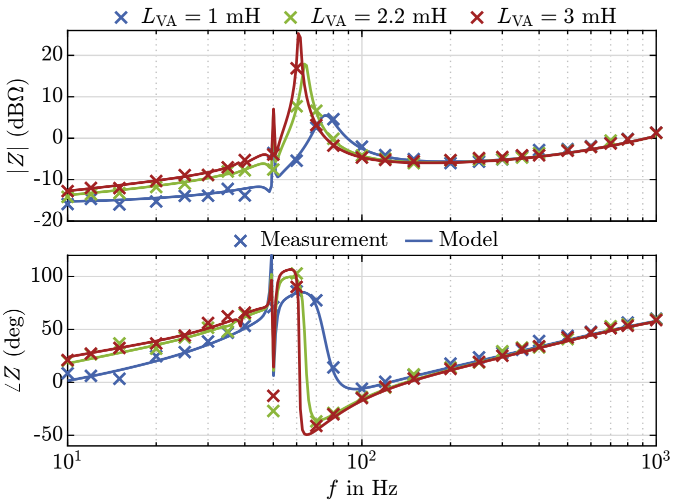

Fig. 9. Measured and modeled positive sequence impedance curves for variation of virtual inductance L_{VA}

This allows for the implementation of differential impedance spectroscopy [22]:

$$Z_{GFM}(s,\varphi) = \frac{v_{PCC}(s,\varphi+120°) - v_{PCC}(s,\varphi)}{i_g(s,\varphi+120°) - i_g(s,\varphi)} \quad (15)$$

This method requires a large number of distinct excitations and measurements. Therefore, an automated procedure is utilized to sweep through the specified frequencies, adjust the necessary setpoints, trigger the oscilloscope, and collect and store the data.

Fig. 8 shows the resulting converter impedance measurements. The impedance model is depicted by solid lines and is in good agreement with the impedance measurements represented by markers, both in phase and magnitude. At 50 Hz, some discrepancy is observed due to the superposition of the excitation signal and the fundamental frequency at this point. Different colors represent variations in the current controller proportional gain $K_{p,cc}$. The impact of this parameter, already discussed in Section II-C and Fig. 6, is confirmed by the measured impedance curves. Another set of measured impedance curves is shown in Fig. 9, where the value of the virtual inductance L_{VA} is varied. Again, the measurements align well with the model and confirm the impact on the impedance peak caused by the virtual admittance.

In Fig. 10, the damping term D_p of the APC is varied. As its effect is confined to the low frequency band, the frequency range is adjusted accordingly. A reduction of D_p results in a stronger response of the internal frequency ω in response to power deviations ΔP, allowing closer tracking of the power setpoint. However, as visible in Fig. 10, this increases the GFM output impedance magnitude, deteriorating its voltage source characteristic. Additionally, for low values of D_p, the non-passive ($|\angle Z| \geq 90°$) region increases, indicating potential instability. The measurement system is able to accurately identify the GFM output impedance for all values of D_p, even in close proximity to the fundamental frequency.

TABLE II
DEFAULT CONTROL PARAMETERS

Parameter	Symbol	Value
Current Control Proportional Gain	$K_{p,CC}$	0.1
Current Control Integral Gain	$K_{i,CC}$	100
Virtual Inductance	L_{VA}	2.2 mH
Virtual Resistance	R_{VA}	100 mΩ
APC Damping Term	D_p	250
Virtual Inertia	J	0.25 kg m^2
Operating Point Voltage	v_0	325 V

IV. Stability Assessment and Mitigation

In this section, the converter impedances obtained through analytical modeling and impedance measurements are used to assess and mitigate the converter interactions observed in two laboratory setups.

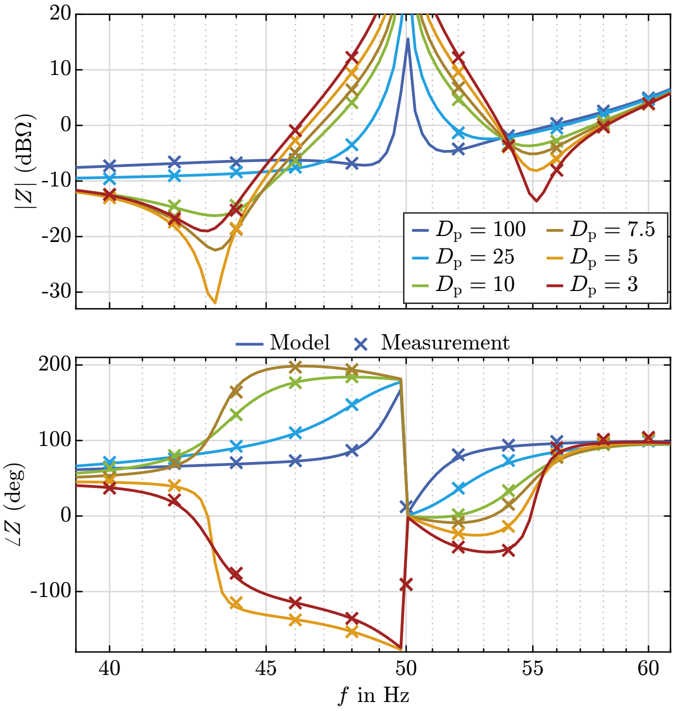

Fig. 10. Measured and modeled positive sequence impedance curves for variation of APC damping term D_p

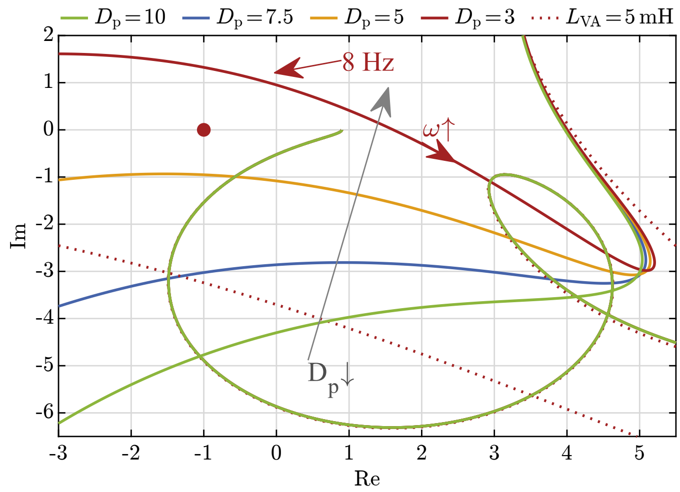

Fig. 11. Nyquist diagrams for the eigenvalues of $L = Z_\mathrm{GFM} Z_\mathrm{Grid}^{-1}$ with variations in damping term D_p

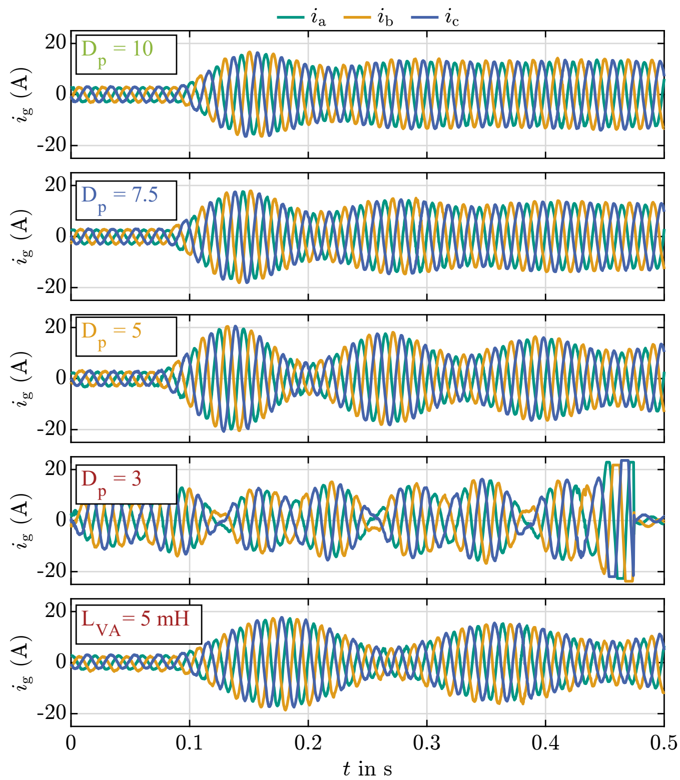

Fig. 12. Measurements of critical and unstable interactions in the GFM-grid setup

A. GFM-Grid Scenario

In the first setup, the GFM converter is connected to a strong grid with $L_\mathrm{g} = 50\,\mu\mathrm{H}$. Due to the MIMO characteristics of the investigated system described in Section II-B, the generalized Nyquist criterion (GNC) is used to assess its stability. In a simplified form and applied to the considered setup, the GNC states that the system is stable if the traces of the frequency-dependent eigenvalues of $L(s) = Z_\mathrm{GFM}(s) Z_\mathrm{Grid}^{-1}(s)$ do not encircle the critical point $(-1, 0)$ [23]. Fig. 11 shows the Nyquist diagram for the resulting eigenvalues. The plot shows that reducing D_p shifts the eigenvalue trace above the critical point, destabilizing the system. A low damping term of $D_\mathrm{p} = 3$ results in instability. The eigenvalue trace is closest to the critical point at a frequency of $f_\mathrm{crit} = 8\,\mathrm{Hz}$. Increasing the virtual inductance L_VA to $5\,\mathrm{mH}$ restores system stability. In this configuration, the trace is closest to the critical point at a frequency of $f_\mathrm{crit} = 5.1\,\mathrm{Hz}$.

The described scenario is examined in a laboratory setup. The resulting measurements of grid currents are shown in Fig. 12. At $t = 0.1\,\mathrm{s}$, the power setpoint is changed to $P_\mathrm{set} = 5\,\mathrm{kW}$. For lower values of D_p, increasing oscillations appear until the converter becomes unstable at $D_\mathrm{p} = 3$ with an oscillation frequency of $7.5\,\mathrm{Hz}$. When the virtual inductance L_VA is increased to $5\,\mathrm{mH}$, stability is restored, and the step response shows a lower oscillation frequency of $5\,\mathrm{Hz}$.

B. GFM-GFL Scenario

In the second laboratory setup, the GFM converter is connected to a grid-following (GFL) converter, which synchronizes with the GFM output voltage and serves as a controllable load. Fig. 13 shows the Nyquist diagram for the resulting eigenvalues. The impedance of the GFL converter is also obtained and validated using the matrix signal-flow graph method [19]. The plot shows that the controller parameters will result in instability when using a low current control gain of $K_\mathrm{p,CC} = 0.25$ for the GFL converter. The eigenvalue trace is closest to the critical point at a frequency of $f_\mathrm{crit} = 14\,\mathrm{Hz}$.

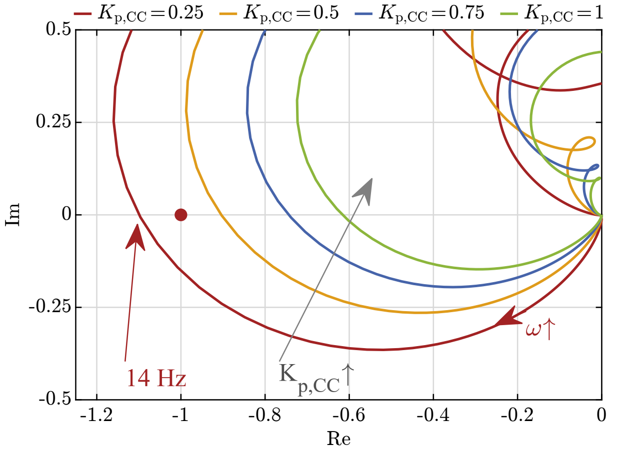

Fig. 13. Nyquist diagrams for the eigenvalues of $L = Z_{\mathrm{GFM}} Z_{\mathrm{GFL}}^{-1}$ with variations in the current controller proportional gain of the GFL converter

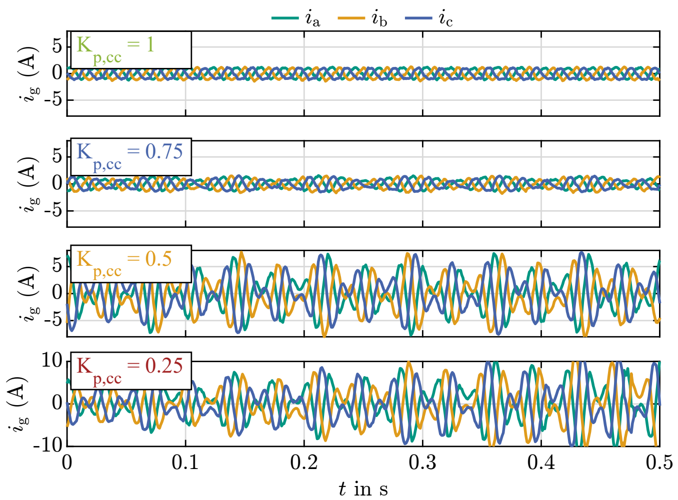

Fig. 14. Measurements of critical and unstable interactions in a GFM-GFL converter system

This matches with the impedance peak caused by the virtual admittance seen in Fig. 9. The eigenvalue trace is closest to the critical point at a frequency of $f_{\mathrm{crit}} = 14\,\mathrm{Hz}$. With $f_0 = 50\,\mathrm{Hz}$, this corresponds to $f_0 + f_{\mathrm{crit}} = 64\,\mathrm{Hz}$, approximately the 65 Hz impedance peak caused by the virtual admittance in Fig. 9. Increasing $K_{\mathrm{p,CC}}$ shifts the eigenvalue trace to the right of the critical point, thus stabilizing the system. The stability assessments for the control configurations investigated analytically in Fig. 13 are validated in a laboratory setup. Fig. 14 shows associated measurements for the considered scenarios. When reducing $K_{\mathrm{p,CC}}$, an oscillation appears at $f_{\mathrm{crit}} = 14\,\mathrm{Hz}$ until the system becomes unstable at $K_{\mathrm{p,CC}} = 0.25$, confirming the analytical stability assessment.

V. Conclusion

This paper presents a detailed impedance model for GFM converters with virtual admittance control, derived using a matrix signal-flow graph. The model includes multiple control loops, and their influences across different frequency ranges are investigated. A measurement setup to determine the impedance of GFM converters is demonstrated. This setup is subsequently used to characterize a test converter and to explore variations in relevant control parameters, thereby verifying the analytical parameter sensitivity analysis. The validated impedance model is then applied to investigate interactions in two experimental setups, providing insights to predict and mitigate measured instabilities.

References

[1] X. Wang and F. Blaabjerg, "Harmonic Stability in Power Electronic-Based Power Systems: Concept, Modeling, and Analysis," *IEEE Transactions on Smart Grid*, vol. 10, no. 3, pp. 2858–2870, May 2019.

[2] J. Sun, "Impedance-Based Stability Criterion for Grid-Connected Inverters," *IEEE Transactions on Power Electronics*, vol. 26, no. 11, pp. 3075–3078, Nov. 2011.

[3] X. Wang, L. Harnefors, and F. Blaabjerg, "Unified Impedance Model of Grid-Connected Voltage-Source Converters," *IEEE Transactions on Power Electronics*, vol. 33, no. 2, pp. 1775–1787, Feb. 2018.

[4] J. Sun, "Frequency-Domain Stability Criteria for Converter-Based Power Systems," *IEEE Open Journal of Power Electronics*, vol. 3, pp. 222–254, 2022.

[5] R. Rosso, X. Wang, M. Liserre, X. Lu, and S. Engelken, "Grid-Forming Converters: Control Approaches, Grid-Synchronization, and Future Trends—A Review," *IEEE Open Journal of Industry Applications*, vol. 2, pp. 93–109, 2021.

[6] J. Yu, S. Wang, Z. Liu, J. Li, J. Liu, and J. Shang, "Accurate Small-Signal Terminal Characteristic Model and SISO Stability Analysis Approach for Parallel Grid-Forming Inverters in Islanded Microgrids," *IEEE Transactions on Power Electronics*, vol. 38, no. 5, pp. 6597–6612, May 2023.

[7] R. Strunk and A. Mertens, "Impedance-Based Stability Analysis of Droop-Controlled AC Microgrids with the Generalized Nyquist Criterion," in *2023 25th European Conference on Power Electronics and Applications (EPE'23 ECCE Europe)*, Aalborg, Denmark: IEEE, Sep. 2023, pp. 1–10.

[8] S. Wang, Z. Liu, and J. Liu, "Modeling of D-Q Small-Signal Impedance of Virtual Synchronous Generator," in *2018 IEEE International Power Electronics and Application Conference and Exposition (PEAC)*, Nov. 2018, pp. 1–6.

[9] Y. Li, Y. Gu, Y. Zhu, A. Junyent-Ferré, X. Xiang, and T. C. Green, "Impedance Circuit Model of Grid-Forming Inverter: Visualizing Control Algorithms as Circuit Elements," *IEEE Transactions on Power Electronics*, vol. 36, no. 3, pp. 3377–3395, Mar. 2021.

[10] X. Wang, F. Blaabjerg, Z. Chen, and W. Wu, "Resonance analysis in parallel voltage-controlled Distributed Generation inverters," in *2013 Twenty-Eighth Annual IEEE Applied Power Electronics Conference and Ex-*

position (APEC), Long Beach, CA, USA: IEEE, Mar. 2013, pp. 2977–2983.

[11] P. Rodriguez, I. Candela, C. Citro, J. Rocabert, and A. Luna, "Control of grid-connected power converters based on a virtual admittance control loop," in *2013 15th European Conference on Power Electronics and Applications (EPE)*, Sep. 2013, pp. 1–10.

[12] L. Huang, C. Wu, D. Zhou, and F. Blaabjerg, "Impact of Virtual Admittance on Small-Signal Stability of Grid-Forming Inverters," in *2021 6th IEEE Workshop on the Electronic Grid (eGRID)*, Nov. 2021, pp. 1–8.

[13] Y. Xiao, H. Ruan, Y. Yang, H. Luo, and F. Blaabjerg, "Experimental Benchmarking of Voltage Controllers for Grid-Forming Inverters," in *2024 IEEE Energy Conversion Congress and Exposition (ECCE)*, Oct. 2024, pp. 1484–1490.

[14] J. D. V. Leon, A. Tarraso, J. I. Candela, J. Rocabert, and P. Rodriguez, "Grid-Forming Controller Based on Virtual Admittance for Power Converters Working in Weak Grids," *IEEE Journal of Emerging and Selected Topics in Industrial Electronics*, vol. 4, no. 3, pp. 791–801, Jul. 2023.

[15] B. Cui, L. Huang, C. Gao, and P. C. Loh, "Virtual Admittance Based Modeling and Stability Analysis of Grid-Forming Inverter under Clark Transformation," in *IECON 2024 - 50th Annual Conference of the IEEE Industrial Electronics Society*, Nov. 2024, pp. 1–6.

[16] P. Zhang, J. Lyu, H. Wang, and X. Cai, "Impedance Modeling and Stability Analysis of VSG-Based Grid-Forming Photovoltaic Inverters," in *2025 IEEE 16th International Symposium on Power Electronics for Distributed Generation Systems (PEDG)*, Jun. 2025, pp. 409–416.

[17] K. Kamalinejad, S. Mohtat, and A. R. Zamani, "Comprehensive derivation of small-signal model for virtual-admittance based grid-forming modular multilevel converters," in *2025 IEEE Energy Conversion Congress and Exposition Europe (ECCE Europe)*, Sep. 2025.

[18] D. Riegle and P. Lin, "Matrix signal flow graphs and an optimum topological method for evaluating their gains," *IEEE Transactions on Circuit Theory*, vol. 19, no. 5, pp. 427–435, Sep. 1972.

[19] D. Schulz, R. Schwendemann, T. Eckstein, A. Liske, and M. Hiller, "Versatile converter impedance modeling with matrix signal flow graphs to include frequency coupling," in *2025 IEEE Energy Conversion Congress and Exposition Europe (ECCE Europe)*, Sep. 2025.

[20] A. Rygg, M. Molinas, C. Zhang, and X. Cai, "A Modified Sequence-Domain Impedance Definition and Its Equivalence to the dq-Domain Impedance Definition for the Stability Analysis of AC Power Electronic Systems," *IEEE Journal of Emerging and Selected Topics in Power Electronics*, vol. 4, no. 4, pp. 1383–1396, Dec. 2016.

[21] S. Frank, D. Schulz, L. Stefanski, R. Schwendemann, and M. Hiller, "A standardized and modular power electronics platform for academic research on advanced grid-connected converter control and microgrids," in *2022 24th European Conference on Power Electronics and Applications (EPE'22 ECCE Europe)*, Sep. 2022, pp. 1–9.

[22] S. Rogalla, S. Kaiser, B. Burger, and B. Engel, "Determination of the Frequency Dependent Thévenin Equivalent of Inverters Using Differential Impedance Spectroscopy," in *2020 IEEE 11th International Symposium on Power Electronics for Distributed Generation Systems (PEDG)*, Sep. 2020, pp. 181–186.

[23] B. Wen, D. Boroyevich, R. Burgos, P. Mattavelli, and Z. Shen, "Small-Signal Stability Analysis of Three-Phase AC Systems in the Presence of Constant Power Loads Based on Measured d-q Frame Impedances," *IEEE Transactions on Power Electronics*, vol. 30, no. 10, pp. 5952–5963, Oct. 2015.